



UNIVERSITY OF LEEDS

This is a repository copy of *Spin-crossover, mesomorphic and thermoelectrical properties of cobalt(II) complexes with alkylated N3-Schiff bases*.

White Rose Research Online URL for this paper:
<http://eprints.whiterose.ac.uk/84884/>

Version: Accepted Version

Article:

Abdullah, N, Noor, NLM, Nordin, AR et al. (7 more authors) (2015) Spin-crossover, mesomorphic and thermoelectrical properties of cobalt(II) complexes with alkylated N3-Schiff bases. *Journal of Materials Chemistry C*, 3 (11). 2491 - 2499. ISSN 2050-7526

<https://doi.org/10.1039/c4tc02923b>

Reuse

Unless indicated otherwise, fulltext items are protected by copyright with all rights reserved. The copyright exception in section 29 of the Copyright, Designs and Patents Act 1988 allows the making of a single copy solely for the purpose of non-commercial research or private study within the limits of fair dealing. The publisher or other rights-holder may allow further reproduction and re-use of this version - refer to the White Rose Research Online record for this item. Where records identify the publisher as the copyright holder, users can verify any specific terms of use on the publisher's website.

Takedown

If you consider content in White Rose Research Online to be in breach of UK law, please notify us by emailing eprints@whiterose.ac.uk including the URL of the record and the reason for the withdrawal request.



eprints@whiterose.ac.uk
<https://eprints.whiterose.ac.uk/>

Spin-crossover, mesomorphic and thermoelectrical properties of cobalt(II) complexes with alkylated N_3 -Schiff bases

Norbani Abdullah,^{*a} Nur Linahafizza Md. Noor,^a Abdul Rahman Nordin,^a Malcolm A. Halcrow,^{*b} Douglas R. MacFarlane,^{*c} Manoj A. Lazar,^c Jennifer M. Pringle,^d Duncan W. Bruce,^{*e} Bertrand Donnio,^{f,g} and Benoît Heinrich^g

Three new cobalt(II) complexes, $[\text{Co}(L^{12})_2](\text{BF}_4)_2$ (**1**), $[\text{Co}(L^{14})_2](\text{BF}_4)_2 \cdot \text{H}_2\text{O}$ (**2**) and $[\text{Co}(L^{16})_2](\text{BF}_4)_2 \cdot \text{H}_2\text{O}$ (**3**), where L^{12-16} are N_3 -Schiff bases appended with linear C_{12-16} carbon chains at the nitrogen atoms, were obtained in good yields by facile one-pot reactions. The single crystal X-ray structure of complex **1** shows a tetragonally compressed CoN_6 coordination geometry. The melting temperatures of **1** – **3** were lower than 373 K, while their decomposition temperatures were above 473 K. All complexes have high-spin Co(II) centres at 300 K and exhibit a columnar mesophase above 383 K. Complexes **1** and **3** showed a normal thermal spin-crossover behaviour with weak hysteresis loops at about 320 K. Hence, these complexes showed uncoupled phase transitions (class iii_a).¹ The values for the Seebeck coefficient (S_e) of the cobalt redox couples formed from **1** and **2** were $1.89 \pm 0.02 \text{ mV K}^{-1}$ and $1.92 \pm 0.08 \text{ mV K}^{-1}$, respectively, identifying them as potential thermoelectrochemical materials.

1. Introduction

The spin-crossover (SCO) phenomenon, where spin states may be switched reversibly between low-spin (LS) and high-spin (HS) configurations by external stimuli such as temperature, pressure and light,²⁻⁶ may be exhibited by complexes of multidentate N - and N,O -donor ligands with first-row transition-metal ions (valence electronic configurations d^4-d^7).^{2,3,7-9} Among these, the most extensively studied SCO materials are complexes of iron(II) (d^6),^{4,10,11} and cobalt(II) (d^7),^{12,13} which have attracted the interest of many researchers as potential functional materials in fields such as molecular electronics, memory storage, thermochromic indicators and sensors.^{14,15} However such applications require that the spin transition occurs abruptly at ambient temperature (ideally room temperature) and with wide thermal hysteresis (for memory effect). These characteristics require strong interactions between the SCO centres, which normally involve van der Waals forces, hydrogen-bonding and π - π interactions.^{14,16}

More recent research on SCO materials now designs them also to have liquid-crystalline properties for the following reasons: facile formation of ordered thin films, enhancement of spin-transition signals, and switching and sensing in different temperature regimes.^{4,17}

At the same time there has been a recent surge of interest in cobalt-based redox couples for both dye-sensitised solar cell (DSSC) and thermoelectrochemical applications. In 2011, the *tris*(2,2'-bipyridine) $\text{Co}^{\text{II/III}}$ redox couple enabled record-breaking 12.3% DSSC efficiencies.¹⁸ More recently another salt of the same Co couple provided record values of the potential change with temperature that is the key to thermoelectrochemical device

applications.¹⁹ For thermal energy harvesting based on the latter devices, research attention has long focused on the $[\text{Fe}(\text{CN})_6]^{3-/4-}$ couple in aqueous systems,²⁰ most recently with respect to the benefits of using high-surface-area electrodes in these devices.^{21,22} The efficacy of a redox couple for thermal energy harvesting depends significantly on the dependence of the redox potential, E , on temperature, which is given by the Seebeck coefficient, $S_e = \partial E / \partial T$. This Seebeck coefficient is related thermodynamically to the entropy change associated with the redox reaction.

The Seebeck coefficient for the benchmark 0.4 M ferri-/ferrocyanide system is 1.4 mV K^{-1} .²³ However, this has recently been surpassed by a 0.01 M solution of *tris*(2,2'-bipyridine) $\text{Co}^{\text{II/III}}$ bis(trifluoromethanesulfonyl)amide (Tf_2N), which achieves up to $2.19 \pm 0.02 \text{ mV K}^{-1}$ in 2-methoxypropionitrile (MPN).¹⁹ The origin of this high Seebeck coefficient is believed to lie in the high-to-low spin transition of the Co centre upon electron transfer, which results in a large redox entropy change. Given these interesting recent developments, and the importance of spin state for the thermal energy harvesting possibilities of cobalt salts, assessment of the physical and thermodynamic properties of a range of other cobalt-based redox couples is of interest to understand the design rules that impact on the Seebeck coefficient. Furthermore, the development of straightforward synthetic techniques is important for improving the accessibility of these materials.

This paper presents structural, spin-crossover, mesomorphic and thermal temperature coefficient studies of three multifunctional, ionic complexes of Co^{II} of general formula $[\text{Co}(L^n)_2](\text{BF}_4)_2$. The complexes were synthesised in one-pot reaction involving $\text{Co}(\text{BF}_4)_2 \cdot 6\text{H}_2\text{O}$, 2,6-pyridinedicarboxaldehyde and $C_n\text{H}_{2n+1}\text{NH}_2$, where $n = 12$ (**1**), 14 (**2**), 16 (**3**). The molecular structure of **1** was

determined by single-crystal X-ray crystallography, while those of **2** and **3** were deduced by comparing their spectral data with those of **1**. Complexes **1** and **2** were then partially oxidised by electrochemical methods to the corresponding Co^{III} redox couples, and the values of their Seebeck coefficients determined.

2. Experimental section

2.1. Materials and general analytical instruments

All chemicals were AnalaR reagents and used as received. Elemental microanalyses were performed by the University of Leeds School of Chemistry microanalytical service. The FT-IR spectra were recorded for neat samples from 4000 cm⁻¹ to 450 cm⁻¹ on a Perkin-Elmer Frontier FT-IR spectrometer equipped with a diamond attenuated total reflectance attachment. The UV-vis spectra were recorded in CHCl₃ from 1200 nm to 400 nm on a Shimadzu UV-vis-NIR 3600 spectrophotometer.

2.2. Syntheses of complexes

2.2.1. [Co(L¹²)₂](BF₄)₂ (1**).** CH₃(CH₂)₁₁NH₂ (0.74 g, 4.0 mmol) was added dropwise to a magnetically stirred solution of 2,6-pyridinedicarboxaldehyde (0.27 g, 2.0 mmol) in methanol (25 ml) at room temperature. Co(BF₄)₂·6H₂O (0.35 g, 1.0 mmol) was then added to the mixture, which was further stirred for 1 h at room temperature. The brick-red powder formed was filtered and washed with diethyl ether. Yield: 0.89 g (76.2%). CHN (%): Calc. C, 63.53; H, 9.46; N, 7.17. Found: C, 63.25; H, 9.45; N, 7.00. ESI-MS: m/z = 498.9 [Co(L¹²)₂]²⁺. FTIR (neat/cm⁻¹): 2918vs, 2852vs, 1592vs, 1471s, 1057vs,br.

2.2.2. [Co(L¹⁴)₂](BF₄)₂·H₂O (2**).** The method was the same as for **1**, using Co(BF₄)₂·6H₂O (0.34 g, 1.0 mmol), 2,6-pyridine-dicarboxaldehyde (0.27 g, 2.0 mmol), and CH₃(CH₂)₁₃NH₂ (0.86 g, 4.0 mmol). The product was a brick-red powder. Yield: 1.16 g (88.8%). CHN (%): Calc. C, 64.56; H, 9.91; N, 6.45. Found: C, 64.9; H, 9.90; N, 6.45. ESI-MS: m/z = 1196.9 {[Co(L¹⁴)₂](BF₄)₂]⁺, 1128.9 {[Co(L¹⁴)₂]F]⁺, 555.0 [Co(L¹⁴)₂]²⁺. FTIR (neat/cm⁻¹): 2918vs, 2852vs, 2513s,br, 2159vs, 2027vs, 1593m, 1468s, 1055s,br.

2.2.3. [Co(L¹⁶)₂](BF₄)₂·H₂O (3**).** The method was the same as for **1**, using Co(BF₄)₂·6H₂O (0.34 g, 1.0 mmol), 2,6-pyridine-dicarboxaldehyde (0.27 g, 2.0 mmol) and CH₃(CH₂)₁₅NH₂ (0.97 g, 4.0 mmol). The product was a brick-red powder. Yield: 1.30 g (92.0%). CHN (%): Calc. C, 66.23; H, 10.26; N, 5.94. Found: C, 66.65; H, 10.30; N, 5.95. ESI-MS: m/z = 1309.1 {[Co(L¹⁶)₂](BF₄)₂]⁺, 611.0 [Co(L¹⁶)₂]²⁺. FTIR (neat/cm⁻¹): 2918vs, 2850vs, 1591m, 1058vs,br, 1467s.

2.3. X-ray crystallography

The single crystal X-ray diffraction data was collected on a Bruker SMART APEX II CCD fitted with Mo K α radiation. The data set was corrected for absorption based on multiple scans²⁴ and reduced using standard methods.²⁵ The structure was solved by direct methods with SHELXS97²⁶ and refined by a full-matrix least-squares procedure on F^2 using SHELXL97 with anisotropic displacement parameters for non-hydrogen atoms and a weighting scheme of the form $w = 1/[\sigma^2(F_o^2) + aP^2 + bP]$, where $P = (F_o^2 + 2F_c^2)/3$. All hydrogen atoms were included in the final refinement in their calculated positions.

2.4. Thermal studies

Thermogravimetry (TG) was carried out on a Perkin-Elmer Pyris Diamond TG/DTA thermal instrument under N₂ at a flow rate of 10 cm³ min⁻¹; the temperature range was 323-1173 K and the scan rate was 20 K min⁻¹. Differential scanning calorimetry (DSC) was done on either a Mettler Toledo DSC 822 calorimeter under N₂ at a flow rate of 20 cm³ min⁻¹ and scan rate 5 K min⁻¹ (for **1** and **2**), or a TA Instruments DSC-Q1000 (for **3**); the scan rates were in a range from 2 to 10 K min⁻¹. The onset temperatures were quoted for all peaks observed.

2.5. Magnetic susceptibility

Magnetic susceptibility at room temperature was determined on a Sherwood automagnetic susceptibility balance by the Gouy method. The instrument was calibrated using Hg[Co(NCS)₄]. Variable-temperature magnetic susceptibility measurements were performed using a Superconducting Quantum Interference Device (SQUID) magnetometer in an applied field of 1000 or 5000 G. Data were acquired in cooling and warming modes, on a 2 K min⁻¹ temperature ramp. A diamagnetic correction for each sample was estimated from Pascal's constants, and a diamagnetic correction for the sample holder was also applied.

2.6. Mesomorphism

Polarising optical microscopy (POM) was carried out on an Olympus polarising microscope equipped with a Mettler Toledo FP90 central processor and a Linkam THMS 600 hot stage. The samples were kept in an oven at 333 K for a few days prior to the analysis to remove absorbed atmospheric moisture. The heating and cooling rates were 10 and 3 K min⁻¹, respectively, and the magnification was 50x.

Small-angle X-ray scattering (SAXS) patterns were obtained with a linear monochromatic Cu K α beam ($\lambda = 1.5405 \text{ \AA}$) obtained using a sealed-tube generator (600 W) equipped with a bent quartz monochromator. Patterns were recorded with a curved Inel CPS 120 counter gas-filled detector linked to a data acquisition computer; periodicities up to 70 \AA can be measured, and the sample temperature controlled to within $\pm 0.01 \text{ K}$ from 293 K to 473 K. Alternatively, patterns were recorded on an image plate; periodicities up to 120 \AA were measured (scanned by STORM 820 from Molecular Dynamics with 50 mm resolution). In all cases, the crude powder was filled in Lindemann capillaries of 1 mm diameter and 10 μm wall thickness and exposure times varied from 1 h to 24 h.

2.7. Seebeck coefficient, S_e

2.7.1. Preparation of cobalt(II/III) redox couple mixture. Measurement of S_e requires the presence of both halves of the cobalt(II/III) redox couple. To synthesise the Co(III) complex, a 0.02 M solution of the Co(II) complex in 3-methoxypropionitrile (MPN), which contained 0.5 M tetrabutylammonium tetrafluoroborate (TBABF₄) as a supporting electrolyte, was oxidised electrochemically using platinum working and counter electrodes. The oxidation and reduction chambers were separated by a frit in order to avoid mixing of the solutions. Chronopotentiometry was used to oxidise the Co(II) to Co(III) until approximately an equimolar mixture of the Co(II) and Co(III) species was produced in the oxidation chamber. The current and the time required for this electrochemical conversion were calculated from Faraday's law and the formation of the 0.01 M Co(II/III) redox couple in MPN was confirmed by cyclic voltammetry.

2.7.2. Measurement of S_e . The S_e values were determined for a 0.01 M solution of the Co(II/III) redox couple in MPN containing 0.5 M TBABF₄. The measurements were done in a non-isothermal cell, as reported previously,²⁷ containing approximately 1 ml of solution. The cell consisted of two compartments – a cold side and a hot side – each containing a platinum wire electrode. The temperature of the cold side was maintained using a water bath. The temperature of the hot side was controlled by insertion of the cell into copper block, which was heated by a cartridge heater and regulated using a temperature controller. The compartments were connected by a salt bridge containing the cobalt redox couple solution. The potential difference between the cold side and the hot side was measured using a Keithley high impedance electrometer. Initially, both compartments were kept at room temperature and a zero potential difference was confirmed. The hot side was then heated by 5 K increments and the potential difference between the two cells was measured. The heating was continued until a temperature difference (ΔT) of 45 – 50 K was obtained. A plot of ΔT vs potential difference gives a straight line, with a slope equivalent to the S_e of the corresponding cobalt redox system.

For comparison, a solution of the previously reported [Co(bipy)₃]^{2+/3+}(Tf₂N)_{2/3} redox couple (0.01 M in MPN, with 0.5 M TBABF₄) was prepared by electrochemical oxidation, and the measured S_e was found to be in good agreement with the literature value.¹⁹

3. Results

3.1. Syntheses and structural deduction

The ionic complexes, [Co(L¹²)₂](BF₄)₂ (**1**), [Co(L¹⁴)₂](BF₄)₂·H₂O (**2**), and [Co(L¹⁶)₂](BF₄)₂·H₂O (**3**), were obtained as brick-red powders in facile one-pot room-temperature reactions involving a methanolic solution of 2,6-pyridinedicarboxaldehyde, Co(BF₄)₂·6H₂O and C_nH_{2n+1}NH₂, where $n = 12, 14$ and 16 , respectively. These complexes were readily soluble in common organic solvents, such as CH₃OH, C₂H₅OH, CHCl₃, CH₂Cl₂, and CH₂(NO₂)₂. The structural formulae of these complexes (Fig. 1) were deduced from a combination of instrumental techniques, and additionally for **1**, by single-crystal X-ray crystallography.

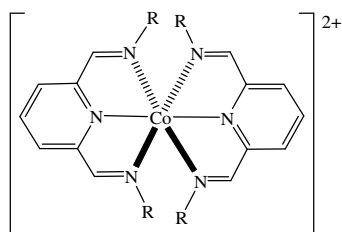


Fig. 1 General structural formula for **1-3** ($R = C_nH_{2n+1}$; $n = 12, 14, 16$). BF₄⁻ ion and lattice H₂O are not shown.

The CHN elemental, ESI-MS and IR data (Experimental) supported the structural formulae of these complexes. Their electronic absorption spectral data in CHCl₃ (Table 1) show $d-d$ bands at about 800 nm and 650 nm, assigned to ${}^4T_{1g}(F) \rightarrow {}^4T_{2g}$ and ${}^4T_{1g}(F) \rightarrow {}^4T_{1g}(P)$ electronic transitions, respectively. These bands support a distorted octahedral geometry at the high-spin (HS) Co^{II} atom in each complex. Three other bands observed were metal-to-ligand charge transfer (MLCT) and intraligand charge transfer. It is interesting to note that the first MLCT

band occurred at quite low energies (about 550 nm) for all complexes.

Table 1 Electronic absorption spectral data for **1-3**

Complex	λ/nm ($\epsilon_{max}/M^{-1} cm^{-1}$)				
	1	822 (100)	650 (229)	549 (1295)	472 (1755)
2	756 (116)	650 (217)	548 (1153)	469 (1604)	384 (2340)
3	815 (104)	648 (226)	550 (1359)	470 (2018)	390 (2823)

Complex **1** formed dark maroon needle-like crystals when the powder was dissolved in methanol followed by slow diffusion in diethyl ether. Single-crystal X-ray crystallography was carried out at 293 K. The crystal data and structure refinement details are given in Table 2, and the selected bond lengths are given in Table 3.

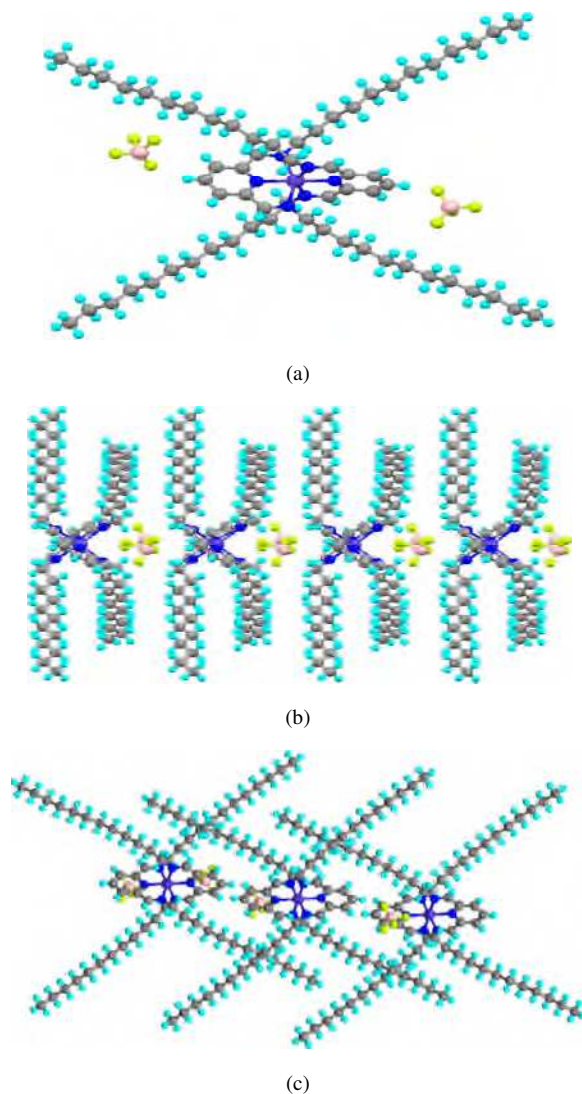


Fig. 2 (a) Molecular structure of **1**; (b) projection showing the cation-anion links; (c) showing interdigitation of the chains and the extension of cation-anion links perpendicular to the chain shown in (b).

The compound crystallised in the monoclinic $P2_1/n$ space group. Its X-ray structure (Fig. 2) reveals that the Co^{II} ion was coordinated by six nitrogen atoms in two L^{12} ligands, while the two BF_4^- counter anions remained uncoordinated. The two L^{12} ligands were nearly perpendicular to one another (making an angle of 79.14°), while both alkyl chains on each ligand were oriented at almost 90° to each other, resulting in a disc-like structure. The two $\text{Co}-\text{N}_{\text{axial}}$ distances (2.038(4) Å) were significantly shorter than the four $\text{Co}-\text{N}_{\text{equatorial}}$ distances (2.217(4) Å). The large difference (0.179 Å) indicates a compressed octahedron, which reflects the rigidity of the tridentate ligand, forcing the pyridyl $\text{Co}-\text{N}$ bonds to be shorter. Other HS Co(II) complexes with related tris-N donor ligands show comparable, but less pronounced, compressed geometries.²⁸⁻³² We are unaware of other published high-spin crystal structures of Co(II) with this type of ligand, but there are some low-spin examples.^{33,34}

The projection of the molecular structure along the bc plane shows significant interaction between the alkyl chains of neighbouring molecules (the fastener effect³⁵). The complexes are held together in a chain-like structure through non-covalent interactions with the BF_4^- anions. This is shown in Fig. 2b, which also shows some 'voids' in the structure (as does Fig. 2a), although these are, however, filled by alkyl chains from adjacent chains of cations and anions through interdigitation (Fig. 2b). Figure 2c shows that cation-anion interactions also exist in the direction perpendicular to the chains of Fig. 2b.

Table 2 Crystallographic data and refinement details of **1**

Empirical formula	$\text{C}_{62}\text{H}_{110}\text{B}_2\text{CoF}_8\text{N}_6$		
Formula weight	1172.11		
Temperature	293 K		
Wavelength	0.71073 Å		
Crystal system, space group	Monoclinic, $P2_1/n$		
Unit cell dimension	$a = 17.1066(3)$ Å	$\alpha = 90^\circ$	
	$b = 9.3515(19)$ Å	$\beta = 107.6370(3)^\circ$	
	$c = 21.8195(2)$ Å	$\gamma = 90^\circ$	
Volume	$3326.39(12)$ Å ³		
Z, Calculated density	2, 1.868 g cm ⁻³		
Absorption coefficient	0.321 mm ⁻¹		
$F(000)$	1266		
θ range for data collection	1.3, 25.0°		
Limiting indices ($\pm h, \pm k, \pm l$)	-20/20, -11/11, -25/25		
Data / restraints / parameters	5851 / 0 / 357		
Goodness-of-fit on F^2	2.24		
Final R indices [$I > 2\sigma(I)$]	$R_1 = 0.0975$, $wR_2 = 0.2831$		

Table 3 Selected bond lengths (Å) for **1**

Co1 – N1	2.216(4)	N1 – C1	1.283(5)
Co1 – N2	2.038(4)	N2 – C2	1.343(6)
Co1 – N3	2.218(4)	N3 – C7	1.262(5)

3.2. Thermal properties

The thermal properties of **1-3** were studied by thermogravimetry (TG) and differential scanning calorimetry (DSC). The data for the major mass losses and strongest peaks are shown in Table 4.

Table 4 TGA and DSC data for **1-3**

Complex	TGA (%)		DSC (T/K) (ΔH / kJ mol ⁻¹)	
	T (K)	Mass loss Found (Calc.)	Heating	Cooling
1	519 - 963	88.2 (91.7)	330.0 (+71.4)	no peak
2	479 - 1073	91.6 (91.2)	347.9 (+68.5)	no peak
3	518 - 930	91.5 (91.9)	360.2 (+48.0)	320.5 (-48.4)

From the TG scans, the major mass losses from each complex were in agreement with the values calculated from loss of two BF_3 and two Schiff base molecules. In addition, complexes **2** and **3** suffered initial mass losses of 1.0 % (temperature range: 358 to 465 K) and 0.9 % (temperature range: 365 to 453 K), respectively, due to evaporation of lattice H_2O . Thus, the thermal stabilities of **1** ($T_{\text{dec}} = 519$ K) and **3** ($T_{\text{dec}} = 518$ K) were similar, and significantly higher than **2** ($T_{\text{dec}} = 479$ K). The trend arose from hydrolyses of the imine bonds for **2** and **3** by the lattice H_2O , and to lower volatility of the hydrolysed products from the Schiff base with a longer alkyl chain.

From DSC, the strongest peaks for all complexes, in the temperature range of 330 K to 360 K, were assigned to Cr-to-mesophase transitions, in agreement with the optical textures observed by polarising optical microscopy (POM), presented below. It is noted that there were no corresponding peaks on cooling for both **1** and **2**, which may indicate slow rate of phase formation. Also, there was a weak endothermic peak for **3** on heating at 336.5 K ($\Delta H = +2.0$ kJ mol⁻¹), assigned to Cr-Cr', which is in agreement with the data from small-angle X-ray scattering (SAXS), also presented below.

3.3. Magnetic susceptibilities

The room-temperature magnetic susceptibilities (χ) for **1-3** were initially measured at 293 K. Complexes **1** and **3** gave almost identical $\chi_{\text{M}}T$ values of 1.9-2.0 cm³ K mol⁻¹, while the value for **2** was lower at 1.5 cm³ K mol⁻¹. Since a fully high-spin Co^{II} complex ($S = 3/2$) typically exhibits $1.5 \leq \chi_{\text{M}}T \leq 2.5$ cm³ K mol⁻¹, and a low-spin Co^{II} complex ($S = 1/2$) shows $\chi_{\text{M}}T \approx 0.45$ cm³ K mol⁻¹,³⁶ it may be inferred that these complexes were mostly high-spin Co^{II} at this temperature. This is consistent with the data from their electronic absorption spectra and variable-temperature magnetic susceptibilities described below.

The variable-temperature magnetic susceptibilities for **1** and **3** were measured using the SQUID magnetometer. The $\chi_{\text{M}}T$ vs T plots are shown in Figs. 3 and 4, respectively. For **1**, the values were determined for two cooling-and-heating cycles. The sample was first cooled from 300 K to 4 K, where $\chi_{\text{M}}T$ first increased gradually from 2.10 cm³ K mol⁻¹ at 300 K to a maximum of 2.40 cm³ K mol⁻¹ at 144 K, and then decreased gradually to 1.48 cm³ K mol⁻¹ at 4 K. This confirms the high-spin nature of the freshly prepared compound (the decrease in $\chi_{\text{M}}T$ at low temperatures is caused by zero-field splitting of the high-spin cobalt ion.^{37,38}) The gradual increase in $\chi_{\text{M}}T$ on cooling between 300-144 K is unusual, but a similar effect has been seen in other high-spin Co(II) complexes of long alkyl chains.³⁹ It may relate to a change in magnetisation caused by a gradual reduction in motion of the alkyl substituents on cooling. When the sample was rewarmed from 4 K, the same pattern of behaviour was observed until a sudden minimum in $\chi_{\text{M}}T$ occurred near 350 K, which is associated with the melting of the sample (see below). A

second thermal cycle of the sample then showed very different, more typical behaviour with an almost continuous decrease in $\chi_M T$ on cooling, from $1.95 \text{ cm}^3 \text{ K mol}^{-1}$ at 372 K to $0.45 \text{ cm}^3 \text{ K mol}^{-1}$ at 4 K. That is consistent with a very gradual spin-equilibrium, of a type that is often exhibited by octahedral Co^{II} complexes.⁴⁰ The compound clearly adopts a different solid phase structure when re-cooled below its melting temperature, which is competent to undergo thermal spin-crossover. A weak hysteretic feature (320-350 K) in the second thermal cycle may also be associated with the compound's melting point.⁴¹

The magnetic behaviour of **3** resembles that of **1** following its melting event. That is, a very gradual decrease in $\chi_M T$ on cooling, from being predominantly high-spin above room temperature to fully low spin below 50 K, consistent with a typically gradual spin-state equilibrium (Fig. 4). The data show a more pronounced thermal hysteresis loop than for **1**, centred near 320 K, which is probably associated with the crystal-liquid crystal transition exhibited by this compound (see below). In contrast to **1**, these show only minor changes upon repeated thermal cycling.

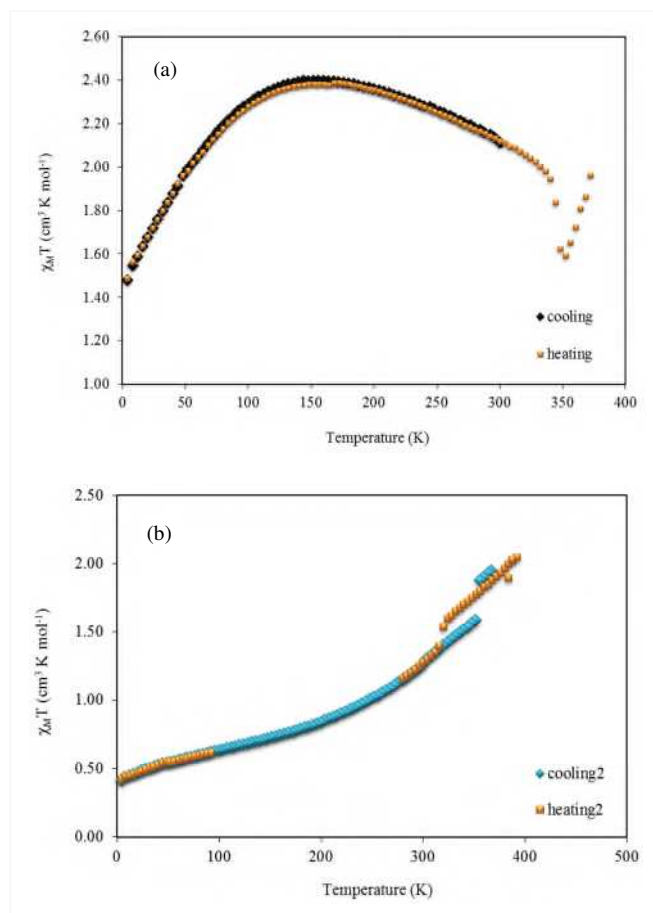


Fig. 3 Plots of $\chi_M T$ vs T for **1**: (a) first cycle (372 K to 4 K); and (b) second cycle (385 K to 4 K)

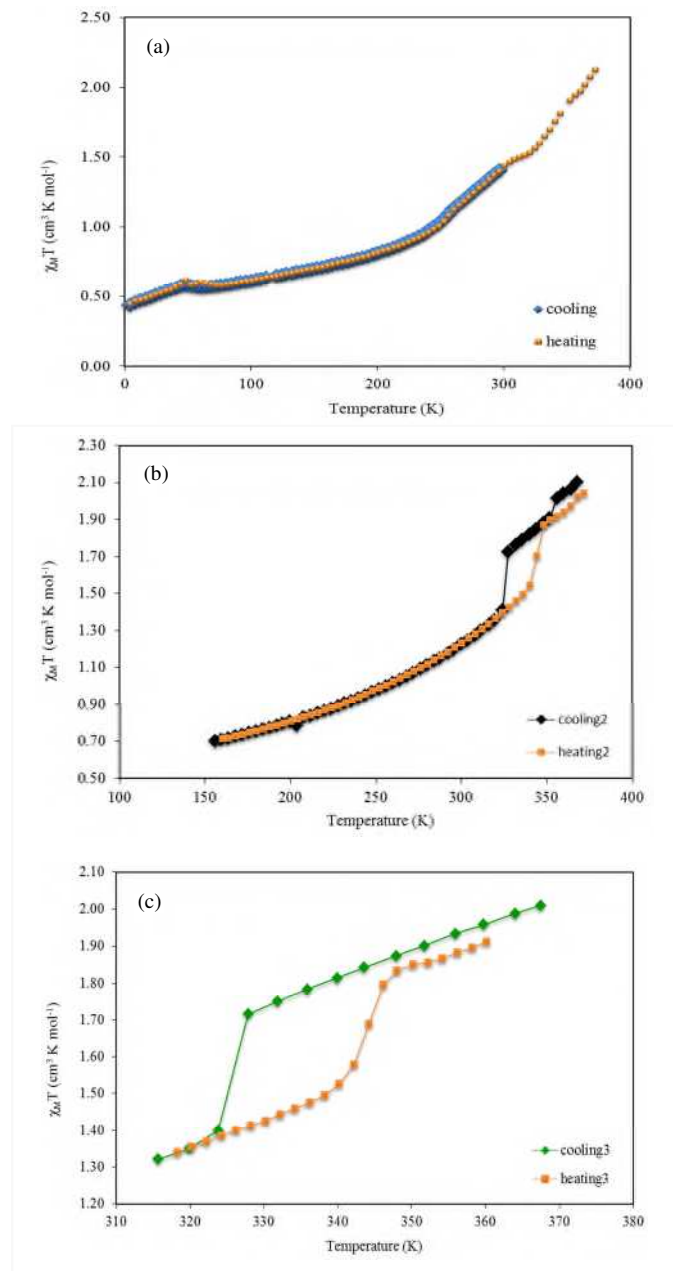


Fig. 4 Plots of $\chi_M T$ vs T for **3**: (a) first cycle (300 K to 5 K); (b) second cycle (370 K to 156 K); and (c) third cycle (370 K to 317 K)

3.4. Mesomorphic properties

The mesomorphic properties of **1-3** were studied by polarising optical microscopy (POM), and additionally for **3**, by small-angle X-ray scattering (SAXS).

By microscopy, **1** was observed to melt at about 343 K and to clear to an isotropic liquid at 420 K. On cooling from the isotropic liquid phase, leaf-like optical texture developed at 413 K, which is characteristic of a columnar (Col) mesophase (Fig. 5(a)). This texture gradually transformed to the spherulite texture of a crystalline phase when cooled further to room temperature.

Similarly, **2** melted at about 348 K and cleared to an isotropic liquid at 437 K. On cooling, an optical texture similar to **1** developed

at 404 K (Fig. 5(b)). This texture then transformed to a broken-fan texture at 390 K.

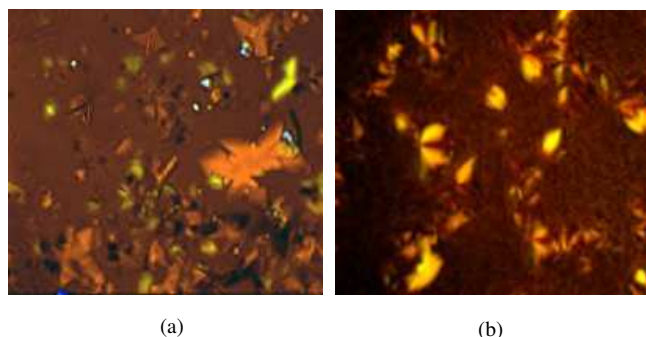


Fig. 5 Photomicrographs of: (a) **1** at 413 K; and (b) **2** at 404 K

Finally, **3** melted at about 353 K. The texture of the mesophase, although the preparation was very dark and was hard to see, resembled that of a columnar phase. The isotropisation (accompanied by decomposition) was detected above 493 K, in agreement with the TG data above (when the complex was heated above this temperature, no mesophase was seen on cooling). The mesomorphism of **3** was then investigated by SAXS. The small-angle patterns, recorded at several temperatures, confirm the microscopy and DSC observations. The mesophase substantially supercooled, and still was present down to 313-323 K, consistent with the absence of a peak for crystallisation in the DSC traces. The transition between the two crystalline phases (Cr and Cr'), while weak by DSC, could be detected by SAXS (slight modifications of peaks number, position, as well as intensity, Fig. 6). Above 373 K, the system develops in a liquid crystal mesophase, with rectangular symmetry (Fig. 7),^{42,43} which remains unchanged throughout the entire temperature domain (Fig. 8), except for a slight expansion of the lattice as the temperature decreased.

The diffraction pattern of the complex recorded in the mesophase at 393 K reveals nine sharp and intense reflections at small values of 2θ ($2^\circ < 2\theta < 16^\circ$, Fig. 7) that permit the unambiguous assignment of a two-dimensional, rectangular lattice, with lattice parameters $a = 45.4 \text{ \AA}$ and $b = 38.4 \text{ \AA}$ (Table 5). In addition, a strong and broad, wide-angle signal with a maximum at *ca* 4.6 \AA was detected, composed of the overlapping of the diffuse scattering arising from lateral distances between molten chains (h_{ch}), which confirmed the liquid-crystalline nature of the mesophase, and another very weak, scattering signal (h_π) at $2\theta \approx 24^\circ$ corresponding to a spacing of about 3.7 \AA . Typically this would result from short-range π - π stacking interactions, but its origin in this case is not clear. The lattice is non-centred, and belongs to the $p2gg$ plane group, as shown by the presence of the reflection 5, (41), ($h + k = 2n + 1$, Table 5 and Fig. 7). The large number of crossed (hk) reflections further show that the electron-rich moieties (ionic metallic fragments) are well organised in the lattice plane and the mesophase results from the well-defined segregation between molten chains and metal complex core (*i.e.* rather sharp interfaces). The presence of three rather intense reflections $h0$ (reflections 2, 4, 6, Fig. 7), suggests that the cobalt pyridine-imine cores are organised into long ribbons, linked through electrostatic interactions with the counter-ions and parallel to the b -lattice direction with a periodicity equal to d_{20} . The strong intensity modulation of these reflections also reveals that these ribbons are not disconnected but in close contact with each other.

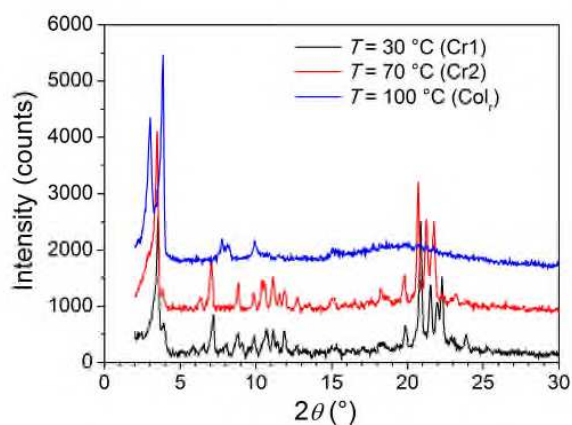


Fig. 6 SAXS patterns recorded in both crystalline phases (Cr and Cr') and mesophase (Col.)

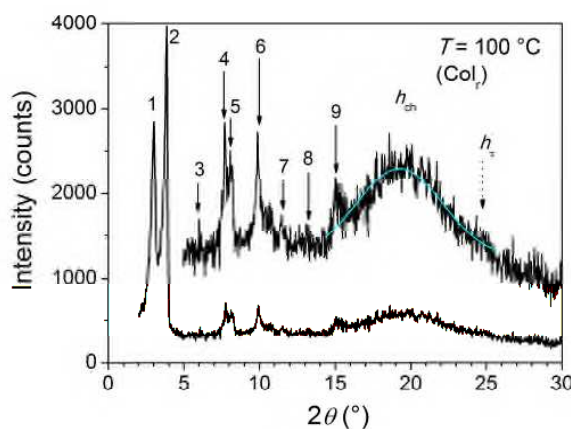


Fig. 7 SAXS pattern of the complex recorded at 373 K in the Col. phase. See peak assignments in Table 5.

The observation of a columnar mesophase in a species with four peripheral chains is not so common, as generally it is regarded that six or more are required in order that the periphery of the core is covered fully by flexible chain. While the chain volume per cation is likely insufficient to provide such coverage, in the single crystal structure this coverage is accomplished *via* interdigitation. We feel that such interdigitation is unlikely in the mesophase, and that the undulations of the ribbons that generate the rectangular network are most likely the consequence of the area mismatch between the alkyl chains and the metal cation (see below). The crystal structure also shows that the cations are bound together into chains *via* electrostatic cation-anion interactions, with the chains being linked again by anions. The well-developed nature of the diffraction pattern suggests strongly that this arrangement persists into the mesophase, accounting for what are evidently well-defined interfaces between the columns.

More quantitatively then, with an estimated volume for the complex, $V_{mol} \approx 2300 \text{ \AA}^3$ ($\rho \approx 1 \text{ g mol}^{-1}$), as calculated from the crystal structure and the volume of the aliphatic chains, a volume equivalent to four complexes ($N = 4$) can be accommodated within a lattice of thickness $h = 5.3 \text{ \AA}$ ($h = NV_{mol}/S$, S being the lattice area, with $S = ab$). Moreover, the area accessible for two chains per complex (only half of the chains of the complex contribute to one

interface), $S_{\text{ch}} \approx 100 \text{ \AA}^2$, ($S_{\text{ch}} = bh/(N/2) = 2bh/N = 2bV_{\text{mol}}/ab = 2V_{\text{mol}}/a$) i.e. about 50 \AA^2 for one chain, deviates too far from the chain cross-section area (22.5 \AA^2). A model for the phase is shown as Fig. 8 which looks along the ribbons (down the c -axis of the rectangular phase).

This model is also in agreement with the molecular parameters: the b -parameter of the rectangular lattice is about twice the lateral periodicity between complexes (see monoclinic structure), whereas the ribbon periodicity ($a/2$) is in the expected range for such a complex.

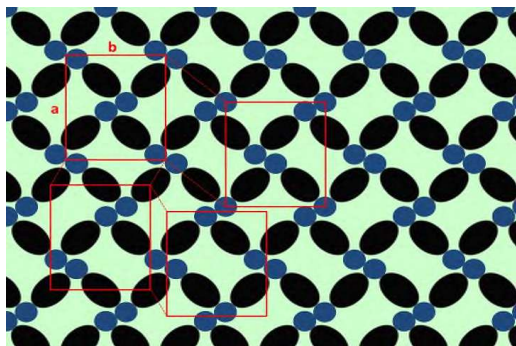


Fig. 8 Proposed model (to scale) for the Col_r phase (the same lattice is shown at different locations). The pale green discontinuous phase represents the alkyl chains, the black ovals the $[\text{Co}(\text{N}_3)_2]^{2+}$ core and the blue discs the BF_4^- anions (only half of the counterions are shown).

Table 5 Indexation of the reflections collected by SAXS at 373 K

Peak	$d_{\text{meas}}/\text{\AA}$	Int./a.u.	Indexation (hk)	$d_{\text{calc}}/\text{\AA}$
1	29.33	vs (sh)	11	-
2	22.70	vs (sh)	20	-
3	14.39	w (sh)	22	14.66
4	11.42	s (sh)	40	11.35
5	10.82	s (sh)	41	10.88
6	8.95	s (sh)	24	8.84
			51	8.83
7	7.63	w (sh)	60	7.57
			15	7.58
8	6.73	w (sh)	35	6.85
9	5.87	m (sh)	73	5.79
			64	5.95
h_{ch}	4.6	vs (br)	-	-
h_{π}	3.55	w (br)	-	-

d_{meas} and d_{calc} are measured and calculated distances; d_{calc} is deduced from the following mathematical expression: $1/d_{hk} = \sqrt{(h^2/a^2 + k^2/b^2)}$; vs, s, m, w, stand for very strong, strong, medium, weak, and correspond to the reflections' intensities; sh and br stand for sharp and broad: a and b are the mesophase lattice parameters.

3.5. Thermochemical properties

The S_e values of the 0.01 M $\text{Co}(\text{II}/\text{III})$ redox couples, with 0.5 M TBABF_4 in MPN, formed by electrochemical oxidation, were determined. Figs. 10 and 11 show the cyclic voltammograms of the cobalt complexes **1** and **2**, respectively, before and after the electrochemical oxidation. It is clear from the current of the first reduction half scans (Figs. 9a and 10a), that as expected the $\text{Co}(\text{III})$ species are absent before the electrochemical oxidation starts. These species are formed during the oxidation process, resulting in an approximately equimolar solution of $\text{Co}(\text{II}/\text{III})$ redox couple; this is confirmed by the current for the oxidation and reduction scans in the

CVs (Figs. 9b and 10b). The peak separation in both cases is >100 mV; however, comparison with similar experiments with a ferrocene/ferrocenium couple in MPN (also >100 mV) suggests that this is chiefly due to uncompensated resistance.

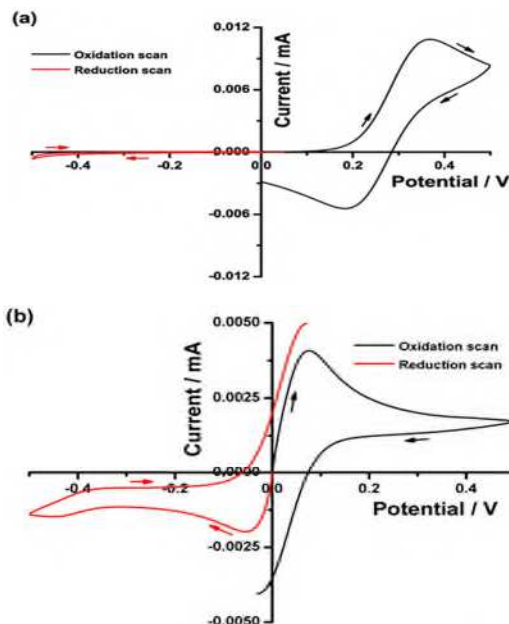


Fig. 9 Cyclic voltammograms of 0.02 M complex **1** in MPN containing 0.5 M TBABF_4 (a) before and (b) after the electrochemical conversion to form Co^{III} . The working, counter and the reference electrodes are platinum.

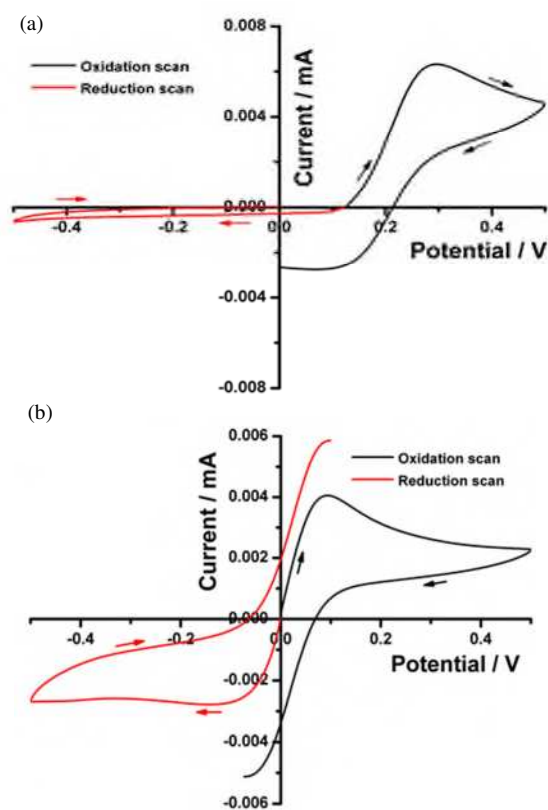


Fig. 10 Cyclic voltammograms of 0.02 M complex **2** in MPN containing 0.5 M TBABF_4 (a) before and (b) after the electrochemical conversion to form Co^{III} . The working, counter and the reference electrodes are platinum.

Fig. 11 shows the result of the S_e determination for complexes **1** and **2**. A linear increase, with a positive slope, was observed between the voltage and temperature difference for both the cobalt complexes in MPN. The S_e values of the cobalt redox couples were determined as $1.89 \pm 0.02 \text{ mV K}^{-1}$ and $1.92 \pm 0.08 \text{ mV K}^{-1}$ for complexes **1** and **2**, respectively. These S_e values exceed the benchmark ferro-/ferricyanide redox system (1.4 mV K^{-1}), but are very close to those reported previously for the $[\text{Co}(\text{bipy})_3]^{2+/3+}[\text{Tf}_2\text{N}]_{2/3}$ cobalt redox couple ($2.19 \pm 0.02 \text{ mV K}^{-1}$).¹⁹

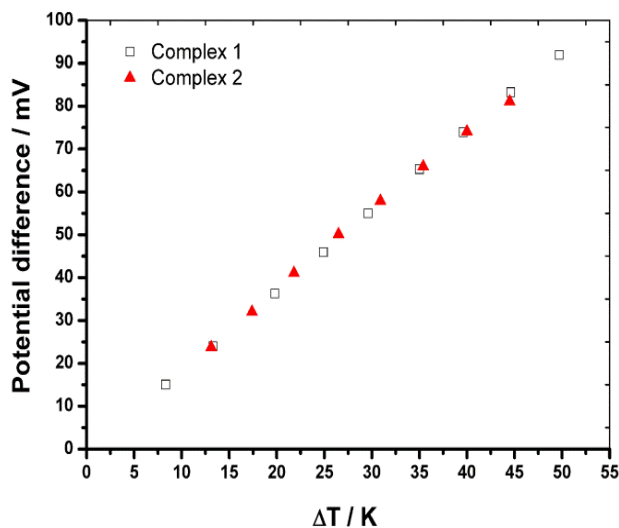


Fig. 11 Seebeck coefficient measurements of 0.01 M $\text{Co}^{\text{III/II}}$ redox couples in MPN containing 0.5 M TBABF₄.

4. Conclusion

Three $\text{Co}(\text{II})$ complexes, $[\text{Co}(\text{L}^{12})_2](\text{BF}_4)_2$ (**1**), $[\text{Co}(\text{L}^{14})_2](\text{BF}_4)_2 \cdot \text{H}_2\text{O}$ (**2**), and $[\text{Co}(\text{L}^{16})_2](\text{BF}_4)_2 \cdot \text{H}_2\text{O}$ (**3**), were obtained as brick-red solids in good yields from facile one-pot reactions involving $\text{Co}(\text{BF}_4)_2 \cdot 6\text{H}_2\text{O}$, 2,6-pyridinedicarboxaldehyde, and $\text{C}_n\text{H}_{2n+1}\text{NH}_2$ ($n = 12, 14, 16$), respectively. Single crystal X-ray crystallography showed that **1** has a tetragonally compressed CoN_6 coordination geometry. All complexes showed low melting temperatures, were thermally stable, had high-spin $\text{Co}(\text{II})$ ions at room temperature, and exhibited a columnar rectangular mesophase. Complexes **1** and **3** showed a normal thermal spin-crossover behaviour with weak hysteresis loops at temperatures below their melting temperatures. Hence, these complexes showed uncoupled phase transitions (class iiiia). Finally, the cobalt redox couples formed from **1** and **2** have similar S_e values ($1.89 \pm 0.02 \text{ mV K}^{-1}$ and $1.92 \pm 0.08 \text{ mV K}^{-1}$, respectively) and hence are potential materials for thermochemical cell applications.

Acknowledgements

The authors wish to acknowledge the Malaysia Ministry of Education for High Impact Research Grant (UM.C/625/1/HIR/MOHE/05) and Fundamental Research Grant Scheme (FP031/2013B), and University of Malaya for Research Grant (RP014A-13AET). Funding from the Australian Research Council for DRM's Australian Laureate Fellowship and support through the Australian Centre for Electromaterials Science is also gratefully acknowledged. BD and BH thank the CNRS for support.

Notes and references

^a Chemistry Department, Science Faculty, Universiti Malaya, 50603 Kuala Lumpur, Malaysia.

^b School of Chemistry, University of Leeds, Leeds, United Kingdom.

^c School of Chemistry, Monash University, Clayton 3800, Australia.

^d ARC Centre of Excellence for Electromaterials Science, Institute for Frontier Materials, Deakin University, Burwood, Victoria, Australia.

^e Department of Chemistry, University of York, Heslington, York YO10 5DD, United Kingdom.

^f Complex Assemblies of Soft Matter Laboratory (COMPASS), UMI 3254 (CNRS-Solvay-University of Pennsylvania), CRTB, 350 George Patterson Boulevard, Bristol, PA 19007, USA.

^g Institut de Physique et Chimie des Matériaux de Strasbourg (IPCMS), UMR 7504 (CNRS-Université de Strasbourg), 23 rue du Loess, BP 43, 67034, Strasbourg, Cedex 2, FRANCE.

† CCDC-1021114 contains the supplementary crystallographic data. These data can be obtained free of charge via <http://www.ccdc.cam.ac.uk/conts/retrieving.html>, or from the Cambridge Crystallographic Data Centre, 12 Union Road, Cambridge CB2 1EZ, UK; fax: (+44) 1223 336033; or e-mail: deposit@ccdc.cam.ac.uk.

- 1 A. B. Gaspar, M. Seredyuk, and P. Gülich, *Coord. Chem. Rev.*, 2009, **253**, 2399-2413.
- 2 O. Kahn, *Molecular Magnetism*, New York: VCH Publishers Inc., 1993.
- 3 P. Gülich, *Spin Crossover in Transition Metal Compounds*, **233**, Berlin-Heidelberg: Springer, 2004.
- 4 Y. Bodenthin, G. Schwarz, Z. Tomkowicz, M. Lommel, T. Geue, W. Haase, H. Möhwald, U. Pietsch, and D. G. Kurth, *Coord. Chem. Rev.*, 2009, **253**, 2414-2422.
- 5 C. Atmani, F. El Hajj, S. Benmansour, M. Marchivie, S. Triki, F. Conan, V. Patinec, H. Handel, G. Dupouy, and C. J. Gómez-García, *Coord. Chem. Rev.*, 2010, **254**, 1559-1569.
- 6 A. B. Gaspar, M. Seredyuk, and P. Gülich, *J. Mol. Struct.*, 2009, **924**, 9-19.
- 7 A. Hauser, C. Enachescu, M. L. Daku, A. Vargas, and N. Amstutz, *Coord. Chem. Rev.*, 2006, **250**, 1642-1652.
- 8 A. B. Gaspar and M. Seredyuk, *Coord. Chem. Rev.*, 2014, **268**, 41-58.
- 9 M. Seredyuk, *Inorg. Chim. Acta*, 2012, **380**, 65-71.
- 10 R.-J. Wei, J. Tao, R.-B. Huang, and L.-S. Zheng, *Eur. J. Inorg. Chem.*, 2013, 916-926.
- 11 S. Heider, H. Petzold, and G. Teucher, *Eur. J. Inorg. Chem.*, 2013, 2382-2388.
- 12 I. Krivokapic, M. Zerara, M. L. Daku, A. Vargas, C. Enachescu, C. Ambrus, P. Tregenna-Piggott, N. Amstutz, E. Krausz, and A. Hauser, *Coord. Chem. Rev.*, 2007, **251**, 364-378.
- 13 S. Hayami, Y. Komatsu, T. Shimizu, H. Kamihata, and Y. H. Lee, *Coord. Chem. Rev.*, 2011, **255**, 1981-1990.
- 14 P. Gutlich, Y. Garcia, and H. A. Goodwin, *Chem. Soc. Rev.*, 2000, **29**, 419-427.
- 15 O. Kahn, *Nature*, 1999, **399**, 21-22.
- 16 P. Gülich, *Metal Complexes*, ed: Springer Berlin Heidelberg, 1981, **44**, 83-195.
- 17 P. G. Bomben, K. C. D. Robson, B. D. Koivisto, and C. P. Berlinguette, *Coord. Chem. Rev.*, 2012, **256**, 1438-1450.
- 18 A. Yella, H.-W. Lee, H. N. Tsao, C. Yi, A. K. Chandiran, M. K. Nazeeruddin, E. W. G. Diau, C. Y. Yeh, S. M. Zakeeruddin, and M. Grätzel, *Science*, 2011, **334**, 629-634.
- 19 T. J. Abraham, D. R. MacFarlane, and J. M. Pringle, *Energy & Environ. Sci.*, 2013, **6**, 2639-2645.
- 20 B. Burrows, *J. Electrochem. Soc.*, 1976, **123**, 154-159.
- 21 R. Hu, B. A. Cola, N. Haram, J. N. Barisci, S. Lee, S. Stoughton, G. Wallace, C. Too, M. Thomas, A. Gestos, M. E. Cruz, J. P. Ferraris, A. A. Zakhidov, and R. H. Baughman, *Nano Lett.*, 2010, **10**, 838-846.
- 22 M. S. Romano, N. Li, D. Antiohos, J. M. Razal, A. Nattestad, S. Beirne, S. Fang, Y. Chen, R. Jalili, G. G. Wallace, R. Baughman, and J. Chen, *Adv. Mater.*, 2013, **25**, 6602-6606.

- 23 T. J. Kang, S. Fang, M. E. Kozlov, C. S. Haines, N. Li, Y. H. Kim, Y. Chen, and R. H. Baughman, *Adv. Funct. Mater.*, 2012, **22**, 477-489.
- 24 G. Sheldrick, SADABS, *University of Göttingen, Germany*, 1996.
- 25 S. APEX, "SADABS; Bruker AXS Inc," *Madison, Wisconsin, USA*, 2007.
- 26 G. Sheldrick, *Acta Crystallogr.: Sect. A*, 2008, **64**, 112-122.
- 27 B. N. Figgis, E. S. Kucharski, and A. H. White, *Aust. J. Chem.*, 1983, **36**, 1537-1561.
- 28 J. M. Holland, C. A. Kilner, M. Thornton-Pett and M. A. Halcrow, *Polyhedron*, 2001, **20**, 2829-2840.
- 29 G. Agusti, C. Bartual, V. Martinez, F. J. Munoz-Lara, A. B. Gaspar, M. C. Munoz, and J. A. Real, *New J. Chem.*, 2009, **33**, 1262-1267.
- 30 C. A. Kilner and M. A. Halcrow, *Dalton Trans.*, 2010, **39**, 9008-9012.
- 31 T. R. Scicluna, B. H. Fraser, N. T. Gorham, J. G. MacLellan, M. Massi, B. W. Skelton, T. G. St Pierre, and R. C. Woodward, *CrystEngComm.*, 2010, **12**, 3422-3424.
- 32 G. Juhasz, S. Hayami, K. Inoue, and Y. Maeda, *Chem. Lett.*, 2003, **32**, 882-883.
- 33 T. J. Abraham, D. R. MacFarlane, R. H. Baughman, L. Jin, N. Li, and J. M. Pringle, *Electrochim. Acta*, 2013, **113**, 87-93.
- 34 C. Förster, K. Mack, L. M. Carrella, V. Ksenofontov, E. Rentschler, and K. Heinze, *Polyhedron*, 2013, **52**, 576-581.
- 35 Y. Komatsu, K. Kato, Y. Yamamoto, H. Kamihata, Y. H. Lee, A. Fuyuhiko, S. Kawata, and S. Hayami, *Eur. J. Inorg. Chem.*, 2012, 2769-2775.
- 36 C. J. O'Connor, *Prog. Inorg. Chem.*, ed: John Wiley & Sons, Inc., 2007, 203-283.
- 37 R. Boča, *Coord. Chem. Rev.*, 2004, **248**, 57-815.
- 38 S. Hayami, M. R. Karim, and Y. H. Lee, *Eur. J. Inorg. Chem.*, 2013, 683-696.
- 39 H. Goodwin, *Transition Met. Compounds I*. 2004, **233**, P. Gütllich, and H. A. Goodwin, Eds., ed: Springer Berlin Heidelberg, 59-90.
- 40 M. Seredyuk, A. B. Gaspar, V. Ksenofontov, Y. Galyametdinov, J. Kusz, and P. Gütllich, *J. Am. Chem. Soc.*, 2008, **130**, 1431-1439.
- 41 M. Seredyuk, A. B. Gaspar, V. Ksenofontov, Y. Galyametdinov, J. Kusz, and P. Gütllich, *Adv. Funct. Mater.*, 2008, **18**, 2089-2101.
- 42 B. Donnio, B. Heinrich, H. Allouchi, J. Käin, S. Diele, D. Guillon, and D. W. Bruce, *J. Am. Chem. Soc.*, 2004, **126**, 15258-15268.
- 43 F. Morale, R. W. Date, D. Guillon, D. W. Bruce, R. L. Finn, C. Wilson, A. J. Blake, M. Schröder, and B. Donnio, *Chem. Eur. J.*, 2003, **9**, 2484-2501.